PAPER

Enhanced methanol oxidation and oxygen reduction reactions on palladium-decorated FeCo@Fe/C core–shell nanocatalysts in alkaline medium

Omobosede O. Fashedemi[a] and Kenneth I. Ozoemena*[ab]

Palladium based nano-alloys are well known for their unique electrocatalytic properties. In this work, a palladium-decorated FeCo@Fe/C core–shell nanocatalyst has been prepared by a new method called *microwave-induced top-down nanostructuring and decoration* (MITNAD). This simple, yet efficient technique, resulted in the generation of sub-10 nm sized FeCo@Fe@Pd nanocatalysts (mainly 3–5 nm) from a micron-sized (0.21–1.5 μm) FeCo@Fe/C. The electrocatalytic activities of the core–shell nanocatalysts were explored for methanol oxidation reaction (MOR) and oxygen reduction reaction (ORR) in alkaline medium. A negative shift of 300 mV in the onset potential for MOR was observed, with a current thrice that of the Pd/C catalysts. A very low resistance to electron transfer (R_{ct}) was observed while the ratio of forward-to-backward oxidation current (I_f/I_b) was doubled. The overpotential of ORR was significantly reduced with a positive shift of about 250 mV and twice the reduction current density was observed in comparison with Pd/C nanocatalysts with the same mass loading. The kinetic parameters (in terms of the Tafel slope (b) = -59.7 mV dec^{-1} (Temkin isotherm) and high exchange current density (j_o) = 1.26×10^{-2} mA cm^{-2}) provide insights into the favorable electrocatalytic performance of the catalysts in ORR in alkaline media. Importantly, the core–shell nanocatalyst exhibited excellent resistance to possible methanol cross-over during ORR, which shows excellent promise for application in direct alkaline alcohol fuel cells (DAAFCs).

1. Introduction

Palladium (Pd)-based electrocatalysts have continued to be a subject of major research interest for application in direct alkaline alcohol fuel cells (DAAFCs).[1–3] There are several reasons for such research interest and they include: (i) Pd is more abundant in nature (currently costs half the price of Pt) and so stands a better chance of replacing the expensive platinum (Pt), (ii) Pd exhibits better kinetics for DAAFCs than Pt catalysts, (iii) reaction dynamics are best facilitated in alkaline media compared to the acidic media, (iv) alcohol cross-over from the anode to the cathode may be minimised since cell conductance is affected by the electro-osmotic drag of hydrated hydroxyl ions. In low temperature DAAFCs, cathode performance losses associated with alcohol crossover arise from the fact that most Pt-based cathode systems are catalytically active for alcohol oxidation under cell operating conditions, leading to a mixed cathode potential. This represents a serious problem as it also influences the ORR negatively.[4] Without doubt, one possible solution to the problem will be found in the development of alternative oxygen reduction catalysts that are inactive to methanol oxidation through modified cathode structure and components. In the above context, there is a need for a Pd-based electrocatalyst that permits efficient alcohol oxidation reaction (AOR) kinetics, oxygen reduction reaction (ORR) kinetics and, importantly, tolerates the presence of alcohol in the cathode side should alcohol cross-over occur during cell operation. Pd-based core shell nanocatalysts are known to enhance ORR activities.

Core–shell nanostructures represent efficient electrocatalysts for use in fuel cells.[5–7] Some of the reasons for the decorating or coating of a core or core–shell nanoparticle with a precious metal such as Pd are to improve the stability, and reduce the consumption of precious materials. For practical applications as catalysts, core–shell nanoparticles with sub-10 nm sizes are preferred,[8] however multi-metallic core–shell nanostructures with sizes less than 10 nm are rarely reported in the literature due to the intrinsic challenges in the synthesis.[9] Core–shell structures have been prepared using techniques such as chemical leaching of the non-noble materials,[10] electrochemical deposition techniques[11] or high temperature annealing.[12,13] Each of these methods has drawbacks which

[a] *Department of Chemistry, University of Pretoria, Pretoria 0002, South Africa*
[b] *Energy Materials, Materials Science and Manufacturing, Council for Scientific & Industrial Research (CSIR), Pretoria 0001, South Africa.*
  E-mail: kozoemena@csir.co.za; Fax: +27 128412135; Tel: +27 128413664

20982 | *Phys. Chem. Chem. Phys.*, 2013, **15**, 20982–20991

This journal is © the Owner Societies 2013

include fabrication of large core–shell nanoparticles with 20–50 nm diameter size.[14]

In a recent communication,[15] we reported the synthesis of Pd-based ternary core–shell nanoparticles (FeCo@Fe@Pd/C) with sub-10 nm diameter size using a facile technique called "*microwave-induced top-down nanostructuring and decoration*" (abbreviated 'MITNAD' for simplicity). The MITNAD technique simply involves the use of fast microwave irradiation for a one-step top-down nanosizing of large-sized soft magnetic FeCo@Fe/C core–shell material (0.21–1.5 μm) to sub-10 nm sized Pd-decorated structure, FeCo@Fe@Pd/C (*ca.* 3–7 nm). In this work, we studied the electrocatalytic properties of this novel core–shell nanocatalyst for fuel cells. The nanocatalysts show significant electrocatalytic properties (compared to some literature reports[16–20]) when used for either of the two crucial electrode reactions of DAAFCs, anodic (methanol oxidation reaction) or cathodic (oxygen reduction reaction). Its ORR onset potential (0.07 V) is more positive than those reported by Kim *et al.* for the Pd-Sn/C[16] and ITO-Pd-Sn series.[17] Superior trends in ORR onset potential, reduction potential and current output are also observed in comparison to Au@Pd core–shell and Au–Pd polycrystalline alloys at a higher electrolyte concentration (1 M KOH) reported by Kuai *et al.*[18]

Liu and co-workers[19] recorded the performance of Au–Pd core–shell nanocatalysts with a loading of 10 μg for the oxidation of methanol in alkaline medium. These catalysts show a better performance in terms of the onset potential for MOR, the oxidation potential, current response and the I_f/I_b ratio (I_f/I_b is a useful index for the catalyst's tolerance to carbonaceous species on the catalyst surface and an indication of oxidation of methanol to CO_2 during the anodic scan) with a lesser loading of 1.3 μg. A better I_f/I_b ratio (4.2) is also observed compared to that (1.89) reported by F. Miao *et al.*[20] for Ni-Pd/Si-MCP nanocomposites for methanol oxidation.

MOR and ORR in alkaline media have been studied using Pd-based catalysts.[16–26] We expect that these newly designed core–shell nanocatalysts can also be used as advanced catalysts to enhance electrocatalytic activity in alkaline fuel cells, further extending their applications in direct alkaline alcohol fuel cells. These catalysts are easy to fabricate, and for ORR, they exhibit fast kinetics which can be judged by their high exchange current density value and low Tafel value and they also show a very high resistance to methanol cross over at high concentrations in the cathode region. On the other hand, they also have a very low resistance to electron transfer coupled with a high I_f/I_b ratio for MOR. This makes them prospective cheaper alternatives to some other palladium based nanocatalysts for DAAFCs.

2. Experimental

The palladium-decorated FeCo@Fe/C core–shell nanoparticles (FeCo@Fe@Pd/C) were prepared as recently described.[15] First, the FeCo/C catalyst was synthesized by a simple reduction method. 0.3650 mg (1.5 mmol) of $CoCl_2 \cdot 6H_2O$ and 0.5302 mg of $FeCl_2 \cdot 4H_2O$ were dissolved in 20 mL of triply-distilled deionized water, and then 150 mg of Vulcan XC-72 carbon

support were dispersed in it. The suspension was ultrasonicated for about 30 min, and then subjected to heating under continuous magnetic stirring until the solvent was completely evaporated to give a smooth, thick slurry. The slurry was oven-dried at 60 °C, and then ground in an agate mortar to give a fine dark and free-flowing powder. The FeCo/C powder was heated in a tube furnace at 300 °C under flowing H_2/Ar for 2 h, and then annealed at 500 °C for 2 h to achieve the core–shell structure (FeCo@Fe/C). The fine powder was left to cool to room temperature under an Ar atmosphere. For "core" and "shell" preferences, note that transition metal with larger cohesive energy and a smaller WS radius prefers the core region, while the metal with smaller cohesive energy and larger atomic size prefers the shell position.[27,28] Because of its larger cohesive energy (4.5 eV) and a smaller atomic size (1.40 Å) than Fe (4.3 eV and 1.47 Å), Co will prefer the core region while Fe migrates to the surface forming a Fe-rich shell. To make the FeCo@Fe@Pd/C nanoparticles, the as-prepared carbon supported FeCo@Fe (1 mmol) was thoroughly mixed with $PdCl_2$ (3 mmol) in ethylene glycol solution containing polyvinylpyrolidone and subjected to rapid microwave irradiation (using the Anton Parr Synthos 3000 microwave reactor) at 500 W, 80 bars, and ~198 °C for 15 min. The resulting product was repeatedly washed with acetone and deionised water to remove traces of ethylene glycol and other impurities, and then dried at 100 °C. As Pd has smaller cohesive energy (3.5 eV) and a larger atomic size (1.55 Å) than Fe (4.3 eV and 1.47 Å), Pd will migrate to the surface forming a Pd-rich shell. For comparison, Pd/C nanoparticles of the same mass loading (3 mmol) as the core–shell were also synthesized using the same microwave procedure. The nanomaterials were thoroughly characterized using XRD (PANalytical X'Pert powder diffractometer with Co Kα radiation), HRTEM and selected area electron diffraction (SAED) (Tecnai F-20 instrument equipped with Gatan HAADF-STEM operated at an accelerating voltage of 200 kV, the Gun extraction voltage was 4500 V). Energy dispersive spectroscopy (EDS) line scan was also performed using this instrument in the STEM mode. Samples for TEM analysis were prepared by dispersing the nanoparticles in methanol, sonicating for 1 min in order to ensure adequate dispersion of the nanostructures, evaporating one drop of the solution onto a 300 mesh Cu grid, coated with a lacey carbon film. SEM images were obtained utilizing a field emission scanning electron microscope (FESEM Zeiss-Leo DSM982). All electrochemical experiments were carried out at room temperature with a conventional three-electrode configuration using an Autolab potentiostat PGSTAT 100 (Eco Chemie, Utrecht, Netherlands) driven by the General Purpose Electrochemical Systems data processing software (GPES and FRA softwares version 4.9). The working electrode was a modified glassy carbon disk electrode (GCE, Bioanalytical systems, diameter = 3.0 mm). A Pt rod and Ag|AgCl, saturated (3 M KCl) were used as a counter and reference electrode, respectively. Electrochemical impedance spectroscopy (EIS) measurements were performed using Autolab Frequency Response Analyser (FRA) software between 100 kHz and 10 mHz with the amplitude (rms value) of the AC signal of 10 mV.

This journal is © the Owner Societies 2013

Phys. Chem. Chem. Phys., 2013, **15**, 20982–20991 | **20983**

All solutions were de-aerated by bubbling pure nitrogen prior to each electrochemical experiment. Before each measurement the GCE was polished to a mirror finish using Alumina slurry (nanopowder Aldrich) and then cleaned by ultrasonic stirring in ethanol and acetone for 3 min, respectively. To prepare the catalyst ink, 1.0 mg of the nanoparticle was dispersed in 1.0 mL of ethanol containing 100 μL of 5% Nafion solution (DuPont). The mixture was ultrasonicated for about 3 min to make a uniform ink. The GCE was modified by dropping 6 μL of the catalyst ink on its surface and allowing it to dry in an oven at about 60 °C. The Pd loading on each electrode was maintained at 1.3 ± 1 μg. Every electrochemical experiment on methanol oxidation was performed in high purity N_2 saturated KOH or KOH containing methanol solutions. For the ORR experiments, 0.1 M KOH solution saturated with high purity oxygen was used, a rotating disk GCE (Autolab Netherlands, 5 mm diameter) was also used.

3. Results and discussion

3.1 SEM, TEM and XRD characterisation

The synthesis procedure is schematically represented in Fig. 1. The precursor FeCo@Fe/C was synthesised by annealing under H_2/Ar conditions at 300–500 °C. A rapid Solvothermal microwave reaction in the presence of palladium (II) salt and ethylene glycol (as a solvent and reductant) was then performed to obtain the Pd-coated FeCo@Fe/C core–shell nanocatalysts. HRTEM analysis showed that the size of FeCo@Fe/C ranged between 0.21 and 1.5 μm (exemplified in Fig. 1), while that of FeCo@Fe@Pd (Fig. 1) is mainly in the 3–7 nm range, further
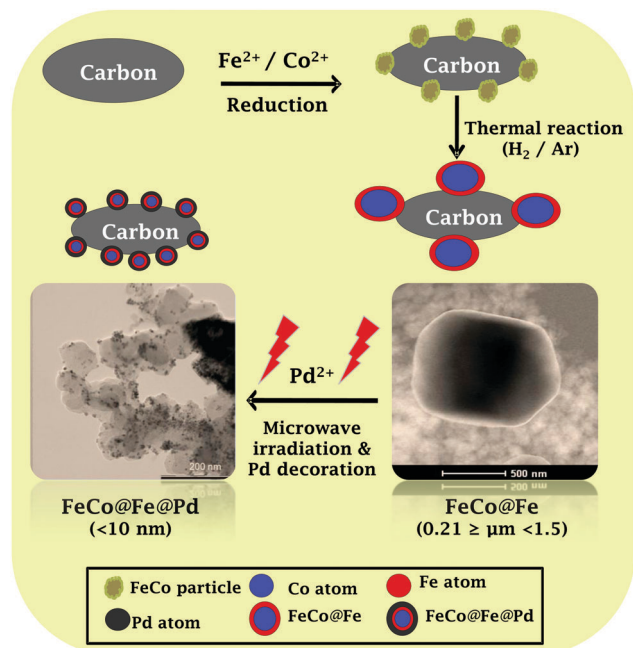

Fig. 2 TEM images of Pd/C (a) and FeCo@Fe@Pd/C (b), with graphs corresponding to their particle size distributions (histograms).

Fig. 1 Schematic representation of the microwave-assisted synthesis of sub-10 nm sized FeCo@Fe@Pd via large-sized FeCo@Fe/C core–shell soft magnetic material.
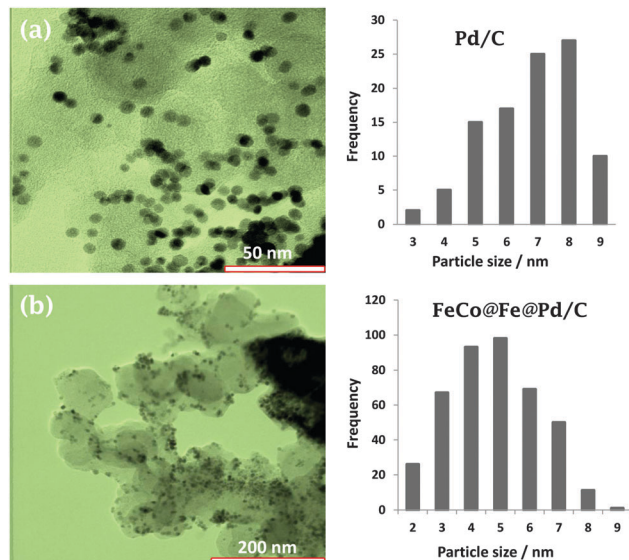
confirmed by the HAADF-STEM image (not shown). Elemental analysis gave the expected stoichiometry as used in the synthesis (a Fe–Co ratio of 2 : 1). Scanning Transmission Electron Microscopy (STEM) was conducted by making use of a high angle annular dark field (HAADF) detector. STEM-EDS revealed that Co is concentrated in the center, while the shell is predominantly Fe. The particle size distributions of the monometallic Pd nanoparticles and FeCo@Fe@Pd core–shell–shell are compared in Fig. 2, proving that the former is slightly larger in size than the latter. This fast formation of the sub-10 nm sized FeCo@Fe@Pd core–shell–shell via microwave irradiation, a "top-down" nanostructuring process, is very interesting as it has never been observed for any noble metal based catalyst. The microwave-enhanced chemistry is hinged upon the efficiency of interaction of molecules with the electromagnetic waves. Unlike the traditional heating process, the temperature of the surrounding in the microwave heating process is colder than that of the target sample (i.e., 'in-core' heating, generated from within the sample). Although the mechanism of microwave–matter interaction is not perfectly understood, it is thought to occur via two physical phenomena: the electric (E) and magnetic (H) field vectors.[29,30] FeCo@Fe is a soft magnetic material with good microwave-absorbing properties.

The microwave solvent used in this study, ethylene glycol (EG), gives the highest 'loss tangent' ($\tan \delta > 0.5$; i.e., the ability of a material to convert electromagnetic energy into heat energy at a given frequency and temperature) compared to other common solvents such as alcohols, water, DMSO or DMF. The excellent microwave-absorbing properties of the EG and FeCo@Fe may explain the fast nanostructuring of this soft magnetic material followed by the Pd coating.

Core–shell preference (i.e., the relative enrichment of a shell by one metal over another) in transition metals is closely linked with the (i) cohesive energy and/or (ii) atomic size, quantified by
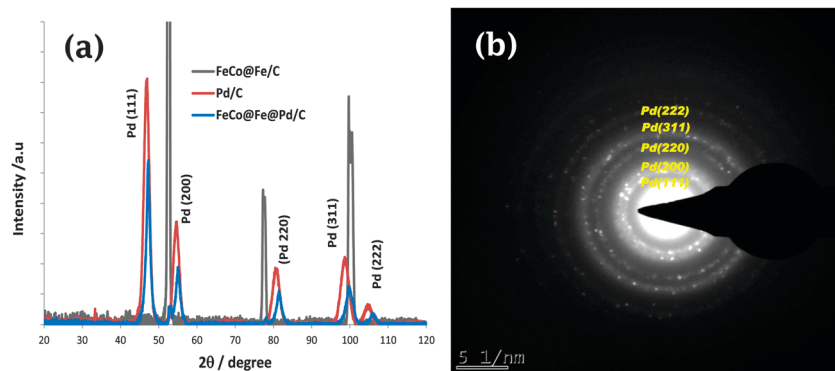
20984 | Phys. Chem. Chem. Phys., 2013, **15**, 20982–20991

This journal is © the Owner Societies 2013

Fig. 3 (a) XRD patterns of Pd/C compared to FeCo@Fe/C and FeCo@Fe@Pd/C; and (b) the SAED pattern of FeCo@Fe@Pd/C.

the Weigner–Seitz (WS) radius. A transition metal with larger cohesive energy and a smaller WS radius prefers to be in the core region. Thus, cohesive energies of 4.5 eV and 4.3 eV with WS radii of 1.4 Å and 1.47 Å for Co and Fe respectively will have Co as the core in the FeCo alloy. Also, an alloy with an Fe-enriched surface combining with Pd with 3.5 eV cohesive energy and WS radius of 1.55 Å will give an alloy with the Fe having a preference for the core region. This explains the structure of FeCo@Fe/C and FeCo@Fe@Pd/C described in this work. The XRD patterns of FeCo@Fe/C and FeCo@Fe@Pd/C are shown in Fig. 3a. The diffraction pattern of the FeCo@Fe/C can be indexed to the body-centered cubic (bcc) structure (SP-type $Pm\bar{3}m$) (JCPDS card: No 03-065-6829). The crystal structure from the TEM and XRD confirmed a bcc. This is in agreement considering that the $Fe_{100-x}Co_x$ alloy exhibits a body-centered cubic structure when $x < 70$ at ~ 730 °C and a face-centered cubic structure at higher temperatures. The intense peaks of the spectrum indicate the crystallinity and the large-sized alloy. FeCo@Fe@Pd/C and Pd/C both display diffraction peaks at 2θ (hkl) values of 46.9° (111), 54.7° (200), 81.1° (220) and 99.4° (311) corresponding to a typical face-centered structure of Pd. The shift of the diffraction lines of Pd in

FeCo@Fe@Pd/C to higher 2θ positions compared to those of Pd/C reflects a lattice contraction as a result of the substitution of the Pd lattice by the FeCo alloy. The lattice strain effect has already been observed for Pd alloys with a Pd-rich surface incorporated with smaller atoms.[31–33] The lattice resolved HRTEM image and the corresponding SAED pattern of the core shell can be seen in Fig. 3b. The interplanar distances from the lattice fringes of the FeCo@Fe@Pd/C nanoparticles lie between 0.231 and 0.248 nm which correspond to the (111) plane of the Pd alloy, in close agreement with the d-spacing of 0.225 nm obtained from the XRD data. A well-defined Pd icosahedron has an interplanar distance of about 0.230 nm between its (111) planes.[34,35]

3.2 CV characterization

Fig. 4 shows the cyclic voltammograms (CV) of the catalysts dispersed on glassy carbon electrode recorded in a N_2 saturated 0.1 M KOH solution. The CV responses show the general features characteristic of palladium. The broad anodic peaks at the potentials of -0.5 V to -0.2 V are associated with the formation of Pd surface oxides, whereas the reduction of these oxides results in a well-defined cathodic peak between -0.4 V
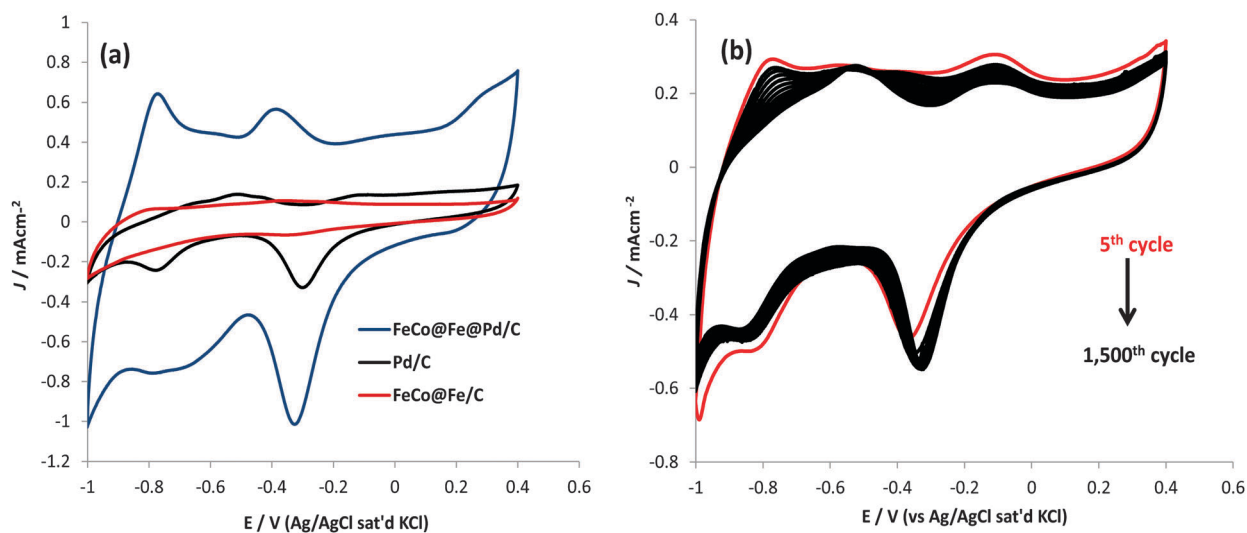

Fig. 4 (a) Comparative cyclic voltammograms of FeCo@Fe/C-core, Pd/C-shell and FeCo@Fe@Pd/C-core shell catalysts in 0.1 M KOH solution saturated with nitrogen. (b) Stability studies with continuous CV cycles in 0.1 M KOH solution saturated with nitrogen: the sweep rate is 50 mV s^{-1}.

This journal is © the Owner Societies 2013

Phys. Chem. Chem. Phys., 2013, **15**, 20982–20991 | **20985**

to −0.3 V. The electrochemically active surface area (EASA) of the Pd catalysts was best estimated using the Pd oxide reduction peak. According to Woods and Rand,[36] the reduction of the Pd monolayer formed on the Pd surface corresponds to a charge density of 0.424 mC cm^{-2}. This provides a convenient method to determine the effective EASA of Pd, without the complications of using the poor hydrogen absorption peak associated with Pd, or surface contamination as observed in other methods e.g., Cu UPD and CO stripping.[37,38] Thus, from Fig. 4, the specific EASA of the nanoparticles modified GCE was estimated using the relation:

$$EASA = \frac{Q}{SI} \quad (1)$$

where Q is the columbic charge (0.0707 and 0.1429 mC for Pd/C and FeCo@Fe@Pd/C, respectively), S is a proportionality constant (0.424 mC cm^{-2}) and I is the catalyst loading 1.3 ± 1 μg (Pd). EASA values were estimated as 149.10 and 245.47 cm^2 mg^{-1} for Pd/C and FeCo@Fe@Pd/C respectively.

3.3 MOR

Fig. 5a compares the cyclic voltammetric responses of methanol oxidation reaction (MOR) at GCE modified with FeCo@Fe/C, Pd/C and FeCo@Fe@Pd/C. The data show that unlike Pd/C and FeCo@Fe@Pd/C, FeCo@Fe/C nanocatalysts did not show any activity towards MOR.

FeCo@Fe@Pd/C showed excellent electrochemical performance compared to Pd/C. It showed a more negative onset potential (−0.5 V) compared to −0.2 V for Pd/C, meaning that it requires lower energy for the MOR to occur on FeCo@Fe@Pd/C than on Pd/C. FeCo@Fe@Pd/C yielded higher current response (∼3 times) than Pd/C. The ratio of the forward anodic peak current density (I_f) to the reverse anodic peak current density (I_b) i.e., (I_f/I_b) is indicative of the ability of the catalyst to tolerate the accumulation of carbonaceous species.[39–43] The I_f/I_b ratios

were estimated as 4.2 and 2.7 for FeCo@Fe@Pd/C and Pd/C, respectively, indicating excellent MOR on the core–shell platform. EIS experiments were performed at −0.2 V to provide further insights into the activities of the two catalysts (Fig. 5b). The size of the semicircle (charge transfer resistance – R_{ct}) in FeCo@Fe@Pd/C is much smaller than that of Pd/C, proving that electron transport is much faster in the former than in the latter.

Fig. 6a shows the linear sweep voltammetric (LSV) evolutions of different concentrations of methanol (0.50–3.0 M range) in 0.5 M KOH on FeCo@Fe@Pd/C at a sweep rate of 1 mV s^{-1}. The current density increased in proportion with the ethanol concentrations until at 1.5 M where it stabilised and then decreased to 3.0 M: approximately from 8 mA cm^{-2} at 1.5 M to 7 mA cm^{-2} at 3.0 M. The methanol oxidation peak potential remained almost constant independent of the concentration, a clear indication of a facile electron transport process, corroborating the EIS data. Fig. 6b shows the dependence of $\log i$ vs. $\log C_{methanol}$ at various fixed potentials (0.38–0.52 V) from a region where the quasi-steady state curves obey the Tafel equation. The slope of the plot ranged between 0.931 and 1.103 indicating that the reaction order is approximately unity, irrespective of potential.

FeCo@Fe@Pd/C shows enhanced catalytic activities for MOR compared to many literature reports[44–53] as shown in Table 1, especially with respect to the onset potential (−0.585 V vs. Ag/AgCl), the J_f/J_b ratio (4.20) and EASA (24.57 m^2 g^{-1}). For example, the Pd-Mn$_3$O$_4$/MWCNT[45] with a larger surface area (76.19 m^2 g^{-1}) showed a lower J_f/J_b ratio (2.60) indicative of a less active MOR in the anodic path compared to FeCo@Fe@Pd/C. Also, interestingly, despite that the loading of the Pd nanoflowers[52] is about 400 times higher than seen for FeCo@Fe@Pd/C, its J_f/J_b ratio (∼5) is comparable with that of FeCo@Fe@Pd/C.

3.4 ORR

The activities of the Pd-based nanocatalysts were also investigated for ORR in 0.1 M KOH. From Fig. 7, it is evident that
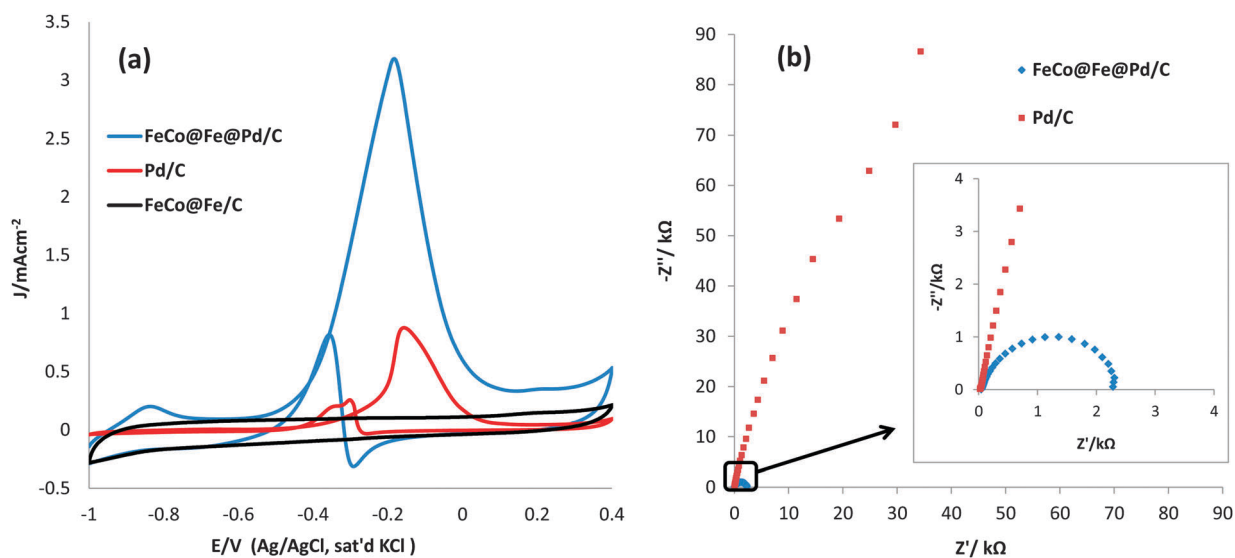

Fig. 5 (a) Comparative cyclic voltammograms of FeCo@Fe/C, Pd/C and FeCo@Fe@Pd/C catalysts in a solution of 0.5 M MeOH/0.5 M KOH. The sweep rate is 25 mV s^{-1}. (b) Nyquists plots of Pd/C and FeCo@Fe@Pd/C at −0.2 V (vs. Ag/AgCl, sat'd KCl) measured in 0.5 M MeOH/0.5 M KOH solution.
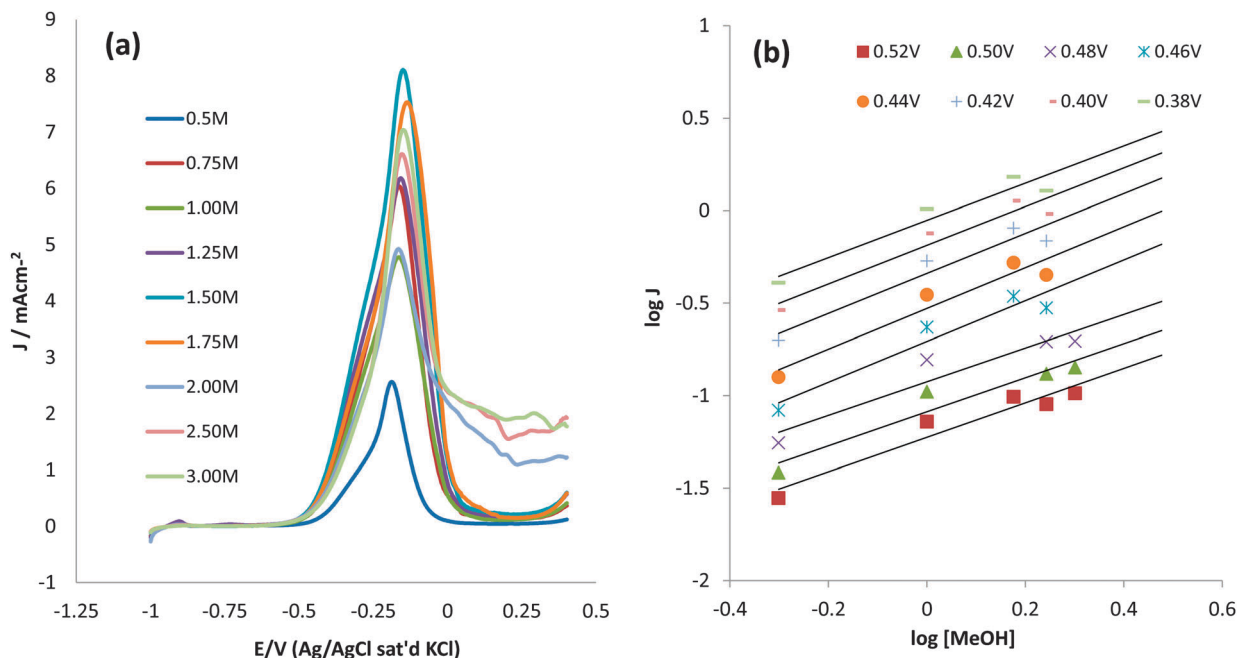
20986 | Phys. Chem. Chem. Phys., 2013, **15**, 20982–20991

This journal is © the Owner Societies 2013

Fig. 6 (a) Linear sweep voltammograms at concentrations of 0.5 M–3.0 M MeOH solutions at 1 mV s^{-1} and (b) plots of log [MeOH] vs. log J.

Table 1 Comparative table showing the catalyst loading, EASA, onset potential (E_{onset}), methanol oxidation potential (E_{peak}) and J_f/J_b values of FeCo@Fe@Pd/C and other catalysts

Catalyst	Electrolyte	Pd loading (μg)	EASA (m^2 g^{-1})	E_{onset} (V)	E_{peak} (V)	J_f/J_b	Ref.
FeCo@Fe@Pd/C	0.5 M MeOH/0.5 M KOH	1.3 (24%)	24.57	−0.585 vs. Ag/AgCl	−0.19	4.20	This work
Ni-Pd/Si-MCP	1 M MeOH/2 M KOH	N/a	9.16	−0.55 vs. SCE	−0.06	1.89	44
Ni-Pd/Si	1 M MeOH/2 M KOH	N/a	3.04	−0.51 vs. SCE	−0.05	N/a	44
Pd-Mn$_3$O$_4$/MWCNT	I M MeOH/0.5 M NaOH	20 wt%	76.19	−0.69 vs. SCE	N/a	2.60	45
Pd/C-nanodots	1 M MeOH/1 M KOH	N/a	N/a	−0.62 vs. Ag/AgCl	∼1.08	∼1.08	46
Pd/HCNF	1 M MeOH/1 M KOH	20.5 wt%	N/a	∼ −0.55 vs. SCE	−0.224	∼3.30	47
Pd/Pani	1 M MeOH/0.5 M NaOH	40	N/a	−0.62 vs. SCE	−0.20 V	∼2.01	48
Pd-Co/CNT (8 : 1)	1 M MeOH/1 M KOH	N/a	N/a	∼ −0.35 vs. Hg/HgO	∼−0.10	1.20	49
CHPN	0.5 M MeOH/0.5 M KOH	1	N/a	∼ −0.50 vs. Ag/AgCl	−0.16 V	3.25	50
PD XC-72 (commercial)	1 M MeOH/1 MNaOH	N/a	N/a	−0.45 vs. Ag/AgCl	∼−0.30	2.50	51
Pd nanoflowers	0.5 M MeOH/0.5 M KOH	500	N/a	∼ −0.19 vs. RHE	0.19	∼5.00	52
Au@Pd/C	0.5 M MeOH/0.5 M KOH	10% metal loading	N/a	∼ −0.50 vs. Ag/AgCl	−0.12	∼3.00	53

Note: CNT – carbon nanotubes, MWCNT – multiwalled carbon nanotubes, Si-MCP – silicon micro channel plates, HCNF – helical carbon nanofibres, PANI – polyaniline nanofibres film, CHPN – carbon nanotube raspberry hollow Pd nanospheres.

FeCo@Fe@Pd/C showed the best ORR activity in terms of onset potential and reduction current density.

The onset potentials are −0.07 V (FeCo@Fe@Pd/C), −0.15 V (Pd/C) and −0.2 V (FeCo@Fe/C), meaning that FeCo@Fe@Pd/C requires the least energy for ORR to occur. Also, the current densities decrease as FeCo@Fe@Pd/C (1.150 mA cm^{-2}) > Pd/C (0.669 mA cm^{-2}) > FeCo@Fe/C (0.046 mA cm^{-2}). Kuai et al.[18] recorded an onset potential of about 0.185 mV with a current density of 0.285 mA cm^{-2} using 1 M KOH for the Au@Pd/C catalyst. FeCo@Fe@Pd/C outperforms this catalyst at much less alkaline concentrations.

Considering the high performance of FeCo@Fe@Pd/C, rotating disk electrode (RDE) experiments were performed to unravel its electro-kinetic properties towards ORR. Fig. 8a compares the hydrodynamic plots of the FeCo@Fe@Pd/C modified GCE in an oxygen-saturated 0.1 M KOH solution at different

rotation rates (from 200 to 2800 rpm), with the current density increasing with increasing rotation rates. The number of electrons involved in the ORR can be obtained from the Koutecky–Levich equation (eqn (2)):[54]

$$\frac{1}{j} = \frac{1}{j_d} + \frac{1}{j_k} = \frac{1}{0.21nFD^{2/3}\gamma^{-\frac{1}{6}}C_{O_2}\omega^{\frac{1}{2}}} + \frac{1}{nFkC_{O_2}} \qquad (2)$$

where j is the measured current, j_d is the diffusion-limiting current, j_k is the kinetic current, n is the number of electrons transferred, F is the Faraday constant, D is the diffusion coefficient (1.95 × 10^{-5} cm^2 s^{-1}), γ is the kinematic viscosity (8.98 × 10^{-3} cm^2 s^{-1}), C_{O_2} is the oxygen concentration (1.15 × 10^{-3} mol dm^{-3}), ω is the rotation speed, and k is the kinetic rate constant. The linearity of the Koutecky–Levich plot (j^{-1} vs. $\omega^{-1/2}$, Fig. 8b) is indicative that the reaction is of a first order, and controlled by kinetics at the

This journal is © the Owner Societies 2013

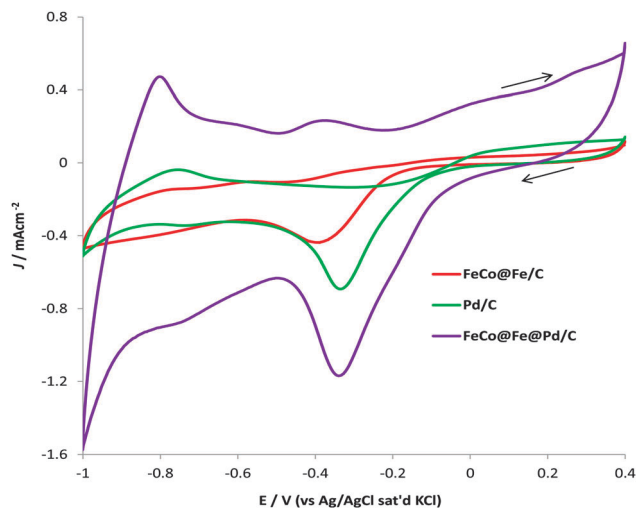*Phys. Chem. Chem. Phys.*, 2013, **15**, 20982–20991 | **20987**

Fig. 7 Comparative cyclic voltammograms of FeCo@Fe/C, Pd/C and FeCo@Fe@Pd/C catalysts in 0.1 M KOH solution saturated with oxygen. The sweep rate is 25 mV s^{-1}.

electrode surface as well as mass transport of oxygen species. From the slope of the plot, the number of electrons (n) transferred per oxygen molecule was calculated as 3.98, suggesting that the ORR process occurs through the direct 4-electron reduction mechanism to produce water as observed for other palladium based alloys. The good linearity and parallelism of the plots are indicative of the first order reaction kinetics with respect to dissolved oxygen. The 4-electron process was also confirmed by the comparison to the slopes of the Koutecky–Levich plot with the theoretical values of 4- and 2-electron reduction processes.

The RDE polarization curves (Fig. 8a) are characteristic of mixed kinetic- and diffusion-controlled currents with no well-defined mass transport-limited current. Similar shapes of

polarization curves were observed in Pd–Ni nanoalloys[55] and Pd$_3$Fe@Pt/C nanocatalysts.[56] This is a feature observed in porous electrodes in which the depth of O$_2$ penetration inside the electrode structure changes with potential. Such features have been attributed to the presence of a polymer or Nafion thin film, thus the kinetic parameters can be estimated from the Koutecky–Levich equation (eqn (2)), assuming the so-called 'two-layer model' (i.e., diffusion in both the polymer/Nafion film used as a catalyst binder and in the hydrodynamic boundary layer).[57,58] Thus the kinetic current (j_k) is defined as in eqn (3)–(5):

$$\frac{1}{j_k} = \frac{1}{|j_o| \exp^{|\eta/b|}} + \frac{1}{j_l^{f-ad}} \tag{3}$$

$$\eta = E - E_{eq} = -b\left(\ln\left|\frac{j_k}{j_l^{f-ad} - j_k}\right| + \ln\left|\frac{j_l^{f-ad}}{j_o}\right|\right) \tag{4}$$

$$\eta = E - E_{eq} = -\frac{RT}{\alpha n F}\left(\ln\left|\frac{j_k}{j_l^{f-ad} - j_k}\right| + \ln\left|\frac{j_l^{f-ad}}{j_o}\right|\right) \tag{5}$$

where j_k is the kinetic current, j_l^{f-ad} is the limiting current due to diffusion through the Nafion film and adsorption on the catalyst particles it is difficult to separate the individual contribution, but the value can be easily estimated from the plot of j_k^{-1} vs. η, see the typical representative plot in Fig. 9a. Having obtained the value of the limiting current (i.e., $j_l^{f-ad} = j_l = 0.323$ mA) we then plotted $\ln(|j_k/(j_l - j_k)|)$ vs. the overpotential (η), which gave a straight line (9b), from the slope of which the Tafel slope b was obtained (59.7 mV dec^{-1}), and from the intercept of which the exchange current density j_o was calculated as 1.26×10^{-2} mA cm^{-2}. The low Tafel slope b (ca. 60 mV dec^{-1}, i.e. RT/F) may be due to the adsorption isotherm of the
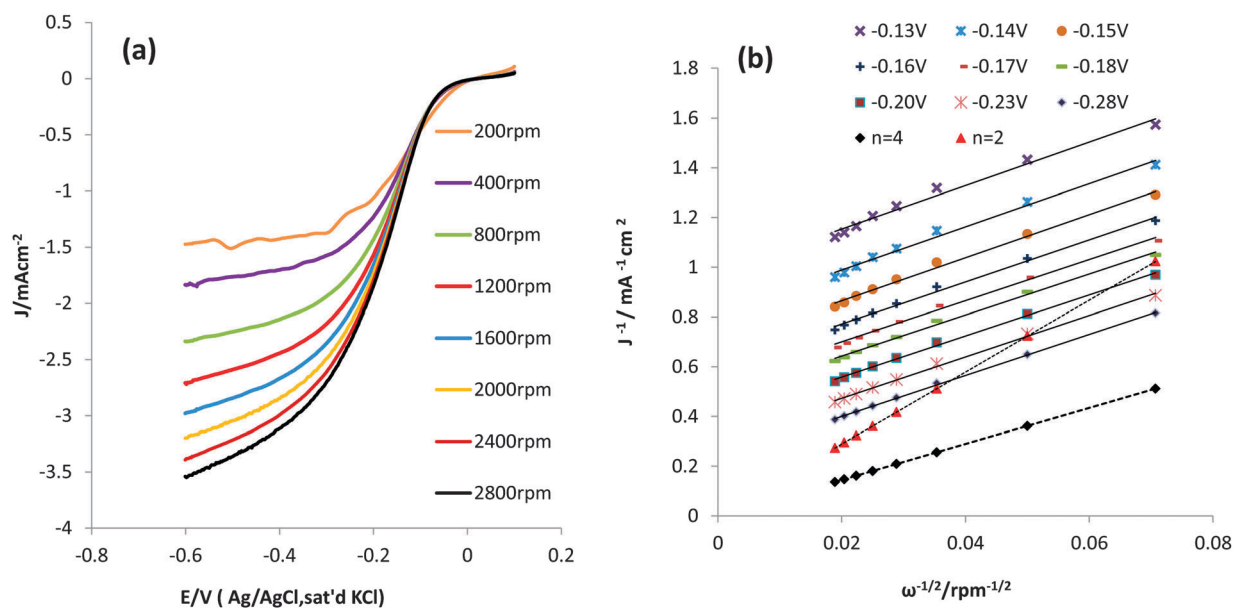

Fig. 8 (a) Hydrodynamic polarization curves of FeCo@Fe@Pd/C in oxygen saturated 0.1 M KOH solution at different rotation rates. (b) Koutecky–Levich plots derived from the hydrodynamic polarization curves.
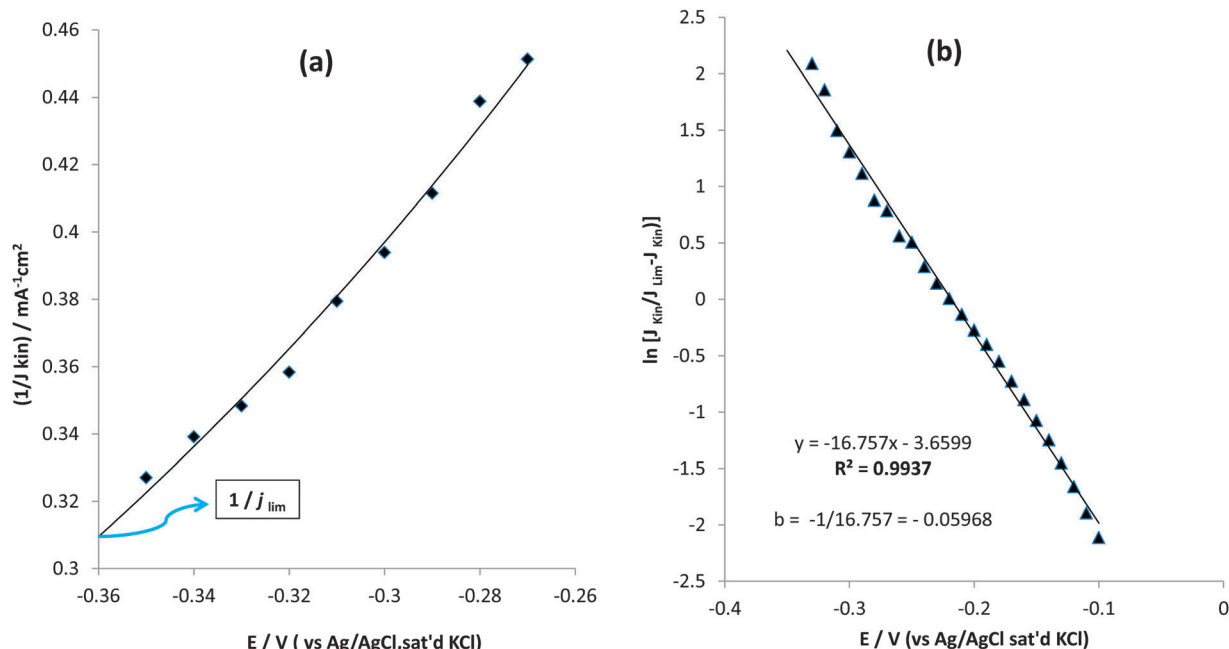
Fig. 9 (a) Plot of J^{-1} vs. η and (b) plot of $\ln(|j_k/(j_l - j_k)|)$ vs. the η.

oxygenated species (Temkin behaviour) as observed by other authors.[59]

Though a considerable controversy still exists about the detailed reaction mechanism in ORR, two main steps governing ORR are: (i) the first electron transfer to the adsorbed oxygen molecule – molecular oxygen dissociation – and (ii) the removal of the adsorbed intermediates (mainly O and OH) formed after the O–O bond rupture.[60,61] The better ORR activity of FeCo@Fe@Pd/C core–shell nanocatalysts can be explained as a result of the combination of both ligand and geometric effects. Here, an electronic shift and geometric strain in the shell due to the underlying core favourably modify the binding energies of reaction intermediates. This occurs particularly in the direct four-electron transfer. The presence of a nanoalloy with an Fe-rich surface, embedded in Pd (with a molar ratio of 1 : 3) will cause a lowering of its oxygen binding energy and thus result in a weak Pd–O/Pd–OH bond. This will improve its ORR activity as a result of the faster kinetics in breaking these bonds. This is consistent with the findings of other authors. Shao et al.[62] conducted a study on some Pd based alloys using the density

functional theory (DFT). Their findings revealed that Pd monolayer on Pd_3Fe (111) has different electronic properties from pure Pd, which causes a large difference in ORR activity between the two surfaces. The latter has a d-band center shifted down by 0.25 eV compared to Pd (111) which significantly lowers the binding energy of O and OH to the surface causing a weakening of Pd–O/Pd–OH bonds and thus a faster removal of O and OH. Pd alloys which bind strongly with O or OH atoms are not expected to be very active because of their slow kinetics in breaking O–O bonds. Additionally, the sluggishness of this step also impedes the adsorption of O_2 as the adsorption sites are occupied by O/OH. The large EASA of FeCo@Fe@Pd/C can also not be left out in explaining its higher ORR catalytic performance. Table 2 compares the performance of FeCo@-Fe@Pd/C with other reports of ORR on Pd-based catalysts.[16,63–66] The data clearly showed that despite the low concentration of the KOH used for the ORR on FeCo@Fe@Pd/C, the reaction still proceeds through the most preferred route for ORR in fuel cells (the 4-electron direct pathway) and at a more positive onset potential compared to many other reports.

Table 2 Comparative table showing onset reduction potential (E_{red} onset), number of electrons transferred and the Tafel slope (b) values of FeCo@Fe@Pd/C and other Pd-based catalysts in ORR

Pd-based catalyst	Electrolyte	E_{red} onset[a] (V)	No of electrons	b (mV dec^{-1})	Ref.
FeCo@Fe@Pd/C	0.1 M KOH	−0.07 vs. Ag/AgCl	3.98	59.8	This work
Pd_3-Ni/C	0.1 M KOH	−0.125 vs. Hg/HgO	3.40	48/110	63
Ag_1Pd_1/CNT	1 M NaOH	−0.1 vs. Ag/AgCl	2.11	N/a	64
Ag_2Pd_1/CNT	1 M NaOH	−0.1 vs. Ag/AgCl	1.88	N/a	64
Ag_4Pd_1/CNT	1 M NaOH	−0.1 vs. Ag/AgCl	2.25	70/136	64
Pd-Sn/C	0.5 M KOH	−0.19 vs. Ag/AgCl	3.8	48/110	16
Pd@Ag/C	0.1 M NaOH	0.0 vs. Hg/HgO	n/a	60/120	66

Note: [a] Onset potential obtained from RDE at 1600 rpm. CNT – carbon nanotube.

This journal is © the Owner Societies 2013

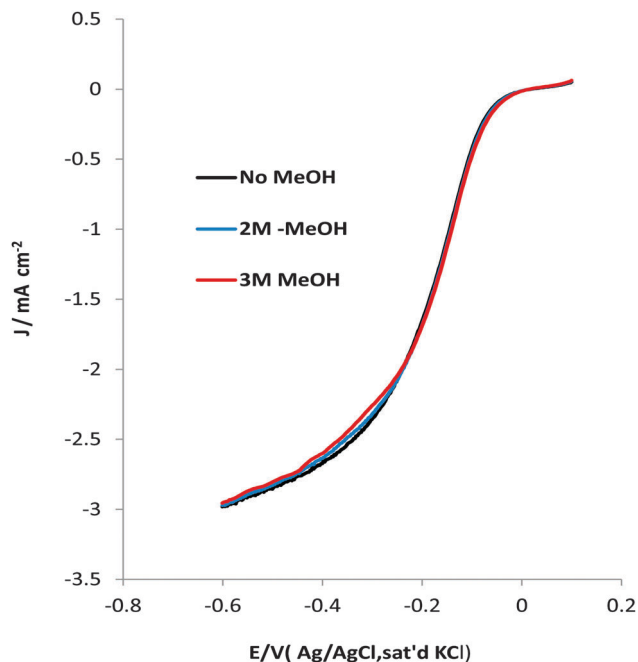Phys. Chem. Chem. Phys., 2013, **15**, 20982–20991 | **20989**

Fig. 10 RDE polarization curves of FeCo@Fe@Pd/C in 0.1 M KOH solution saturated with oxygen and with additions of 2 M and 3 M MeOH at 1600 rpm.

Methanol cross-over in fuel cells is a very serious problem that leads to high overvoltage, impacting negatively on the ORR activities.[60] Therefore, there has always been the need to understand the impact of methanol in ORR. The ORR activity of FeCo@Fe@Pd/C catalysts was evaluated in the presence of different molar concentrations of methanol (Fig. 10). Interestingly, there was no obvious negative shift in the onset potentials or in the current density in the presence of 2 M and 3 M methanol. This shows there is no negative influence of methanol on the FeCo@Fe@Pd/C core–shell nanocatalyst as it exhibits a good tolerance to the presence of high concentrations of methanol.

4. Conclusions

In summary, a facile method has been developed to produce novel FeCo@Fe@Pd/C core–shell nanocatalysts by assisted microwave irradiation. The FeCo@Fe@Pd/C core–shell nanocatalysts show enhanced electrocatalytic activities for methanol oxidation as well as oxygen reduction reaction in alkaline media. The overall performance of FeCo@Fe@Pd/C in MOR and ORR is much greater than observed for Pd/C with the same Pd loading. This high electrocatalytic performance of FeCo@-Fe@Pd/C is related to its core–shell nature as well as its smaller particle size distribution compared to the monometallic Pd/C. Its enhanced activity towards ORR can be due to the favorable lattice strain effects between the Pd shell and the FeCo@Fe core. It affords a moderate bond with oxygen which balances well the two competing influences in ORR (O–O bond breaking and the removal of O and OH). Coupled with its good methanol tolerance, FeCo@Fe@Pd/C can serve as a less expensive

alternative to other palladium based nanocatalysts for DAAFC applications.

References

1 V. Mazmuder, M. Chi, M. N. Mankin, Y. Liu, O. Metin and D. Sun, *Nano Lett.*, 2012, **12**, 1102–1106.
2 Y. W. Lee, M. Kim, Y. Kim, S. W. Kang, J. H. Lee and S. W. Han, *J. Phys. Chem. C*, 2010, **114**, 7689–7693.
3 C. Zhu, S. Guo and S. Dong, *J. Mater. Chem.*, 2012, **22**, 14851–14855.
4 C. Jeyabharathi, P. Venkateshkhumar, J. Mathiyarasau and K. L. N. Phani, *J. Electrochem. Soc.*, 2010, **157**, 1740–1745.
5 W. Tang and G. Henkelman, *J. Chem. Phys.*, 2009, **230**, B194504–B194509.
6 M. Zhang, Z. Yan, Q. Sun, J. Xie and J. Jing, *New J. Chem.*, 2012, **36**, 2533–2540.
7 W. Wang, R. Wang, S. Ji, H. Feng, H. Wang and Z. Lei, *J. Power Sources*, 2010, **195**, 3498–3503.
8 H. Yang, *Angew. Chem., Int. Ed.*, 2011, **50**, 2674–2676.
9 Z. M. Peng and H. Yang, *Nano Today*, 2009, **4**, 143–164.
10 R. Srivastava, P. Mani, N. Hahn and P. Strasser, *Angew. Chem.*, 2007, **119**, 9146–9149.
11 J. X. Wang, H. Indana, L. Wu, Y. Zhu, Y. Choi, P. Liu, W.-P. Zhou and R. R. Adzic, *J. Am. Chem. Soc.*, 2009, **47**, 17298–17302.
12 S. Koh, J. Leisch, M. F. Toney and P. Strasser, *J. Phys. Chem. C*, 2007, **111**, 3744.
13 L. Zhang, K. Lee and J. Zhang, *Electrochim. Acta*, 2007, **52**, 3088–3094.
14 J. Zhang, F. H. B. Lima, M. H. Shao, K. Sasaki, J. X. Wang, J. Hanson and R. R. Adzic, *J. Phys. Chem. B*, 2005, **109**, 22701–22704.
15 O. O. Fashedemi, B. Julies and K. I. Ozoemena, *Chem. Commun.*, 2013, **49**, 2034–2036.
16 J. Kim, T. Momma and T. Osaka, *J. Power Sources*, 2009, **189**, 909–915.
17 J. Kim, J. E. Park, T. Momma and T. Osaka, *Electrochim. Acta*, 2009, **54**, 3412–3418.
18 L. Kuai, X. Yu, S. Wang, Y. Sang and B. Geng, *Langmuir*, 2012, **28**, 7168–7173.
19 Z. Liu, B. Zhao, C. Guo, Y. Sun, F. Xu, H. Yang and Z. Li, *J. Phys. Chem. C*, 2009, **113**, 16766–16771.
20 F. Miao, B. Tao, L. Sun, T. Liu, J. You, L. Wang and P. K. Chu, *J. Power Sources*, 2010, **195**, 146–150.
21 G. Hu, F. Nitze, T. Sharifi, H. R. Barzegar and T. Wagberg, *J. Mater. Chem.*, 2012, **22**, 8541–8548.
22 M. Jafarian, M. A. Haghighatbin, F. Global, M. G. Mahjani and S. Rayati, *J. Electroanal. Chem.*, 2011, **663**, 14–23.
23 H. Sun, X. Jiao, H. Wang, Z. Jiang and D. Chen, *ACS Appl. Mater. Interfaces*, 2011, **3**, 2425–2430.
24 M. H. Seo, S. M. Choi, H. J. Kim and W. B. Kim, *Electrochem. Commun.*, 2011, **13**, 182–185.
25 C. Zhu, S. Guo and S. Dong, *Chem.–Eur. J.*, 2013, **19**, 1104–1111.
26 N. Alexeyeva, A. Sarapu, K. Tammeveski, F. J. Vidal Iglesia and J. Solla, *Electrochim. Acta*, 2011, **56**, 6702–6708.

20990 | *Phys. Chem. Chem. Phys.*, 2013, **15**, 20982–20991

This journal is © the Owner Societies 2013

27 L.-L. Wang and D. Johnson, *J. Am. Chem. Soc.*, 2009, **131**, 14023–14029.

28 Y. Suo, L. Zuang and J. Lu, *Angew. Chem., Int. Ed.*, 2007, **46**, 2862–2864.

29 R. Roy, D. Grawal, J. Cheng and S. Gedevanishvili, *Nature*, 1999, **399**, 668–670.

30 R. Roy, R. Peelamedu, L. Hurtt, J. Cheng and D. Agrawal, *Mater. Res. Innovations*, 2002, **3**, 128–140.

31 J. Zhao, A. Sakar and A. Manthiram, *Electrochim. Acta*, 2010, **55**, 1756–1765.

32 Y. C. Wei, T. Y. Chen, C. W. Liu, T. S. Chan, J. F. Lee, C. H. Lee, T. L. Lin and K. W. Wang, *Catal. Sci. Technol.*, 2012, **2**, 1654–1664.

33 D. Wang, H. L. Xin, Y. Yu, H. Wang, E. Rus, D. A. Muller and H. D. Abruna, *J. Am. Chem. Soc.*, 2010, **132**, 17664–17666.

34 Y. Yu, Y. Zhao, T. Huang and H. Liu, *Pure Appl. Chem.*, 2009, **81**, 2377–2385.

35 Y. Chen, B. He, T. Huang and H. Liu, *Colloids Surf., A*, 2009, **38**, 145–150.

36 D. A. J. Rand and R. Woods, *J. Electroanal. Chem.*, 1971, **31**, 29–38.

37 W. J. Zhou and J. Y. Lee, *J. Phys. Chem. C*, 2008, **112**, 3789–3793.

38 C. J. Zhong, J. Luo, B. Fang, B. N. Wanjala, P. N. Njoki, R. Loukrakpam and J. Yin, *Nanotechnology*, 2010, **21**, 062001.

39 C. L. Lee, H. P. Chiou, C. M. Syu, C. R. Liu, C. C. Yang and C. C. Syu, *Int. J. Hydrogen Energy*, 2011, **36**, 12706–12714.

40 K. J. Mayrhofer, D. Strmicnik, B. B. Blizanac, V. Stamenkovic, M. Arenz and N. M. Markovic, *Electrochim. Acta*, 2008, **53**, 3181–3188.

41 W. Liu, A. K. Herrmann, D. Geiger, L. Borchardt, F. Simon, S. Kaskel, N. Gaponik and E. Eychmuller, *Angew. Chem., Int. Ed.*, 2012, **51**, 5743–5747.

42 N. W. Maxakato, K. I. Ozoemena and C. J. Arendse, *Electroanalysis*, 2010, **22**, 519–529.

43 C. Qiu, R. Shang, Y. Xie, Y. Bu, C. Li and H. Ma, *Mater. Chem. Phys.*, 2010, **120**, 323–330.

44 F. Miao, B. Tao, L. Sun, T. Liu, J. You, L. Wang and P. K. Chu, *J. Power Sources*, 2010, **195**, 146–150.

45 Y. Zhao, S. Ne, H. Wang, J. Tian, Z. Ning and X. Li, *J. Power Sources*, 2012, **218**, 320–330.

46 W. Wei and W. Chen, *J. Power Sources*, 2012, **204**, 85–88.

47 G. G. Hu, F. Nitze, T. Sharif, H. R. Barzegar and T. Wagberg, *J. Mater. Chem.*, 2012, **22**, 8541–8548.

48 R. K. Pandey and V. Lakshminarayanan, *J. Phys. Chem. C*, 2009, **113**, 21569–21603.

49 Y. Wang, X. Wang and C. M. Li, *Appl. Catal., B*, 2010, **99**, 229–234.

50 Z. Liu, B. Zhao, C. Guo, Y. Sun, Y. Shi, H. Yang and Z. Li, *J. Colloid Interface Sci.*, 2010, **351**, 233–238.

51 L. Gao, W. Yue, S. Tao and L. Fan, *Langmuir*, 2013, **29**, 957–964.

52 Z. Yin, H. Zheng, D. Ma and X. Bao, *J. Phys. Chem. C*, 2009, **113**, 1001–1005.

53 Z. Liu, B. Zhao, C. Guo, Y. Sun, F. Xu, H. Yang and Z. Li, *J. Phys. Chem. C*, 2009, **113**, 16766–16771.

54 J. A. Bard and I. Faukner, *Electrochemical Methods, Fundamental and Applications*, Wiley, New York, 2001, pp. 341–344.

55 J. Zhao, A. Sakar and A. Manthiram, *Electrochim. Acta*, 2010, **55**, 1756–1765.

56 W. Wang, R. Wang, S. Ji, H. Feng, H. Wan and Z. Lei, *J. Power Sources*, 2010, **195**, 3498–3503.

57 T. J. Schmidt, H. A. Gasteiger and R. J. Behm, *J. Electrochem. Soc.*, 1999, **146**, 1296–1304.

58 C. Coutanceau, M. J. Croissant, T. Napporn and C. Lamy, *Electrochim. Acta*, 2000, **46**, 579–588.

59 H. Erikson, A. Kasikov, C. Johans, K. Konturi, K. Tammeveski and A. Sarapuu, *J. Electroanal. Chem.*, 2011, **652**, 1–7.

60 C. Song and J. Zang, *PEM Fuel Cell Electrocatalysts and Catalyst Layers: Fundamentals and Applications*, Springer, 2008.

61 X. Yang, J. Hu, J. Fu, R. Wu and B. E. Koel, *Angew. Chem.*, 2011, **123**, 10364–10367.

62 M. Shao, P. Liu, J. Zhang and R. Adzic, *J. Phys. Chem. B*, 2007, **111**, 6772–6775.

63 B. Li and J. Prakash, *Electrochem. Commun.*, 2009, **11**, 1162–1165.

64 C. L. Lee, H. P. Chiou, K. C. Chang and C. H. Huang, *Int. J. Hydrogen Energy*, 2011, **36**, 2759–2764.

65 L. Jiang, A. Hsu, D. Chu and R. Chen, *Electrochim. Acta*, 2010, **55**, 4506–4511.

66 Z. Wen, J. Liu and J. Li, *Adv. Mater.*, 2008, **20**, 743–747.

This journal is © the Owner Societies 2013

Phys. Chem. Chem. Phys., 2013, **15**, 20982–20991 | **20991**